

GE, B., WANG, J., SUN, Y., GUO, J., FERNANDEZ, C. and PENG, Q. 2020. Heterojunction-composited architecture for Li–O₂ batteries with low overpotential and long-term cyclability. *ACS applied energy materials* [online], 3(4), pages 3789-3797. Available from: <https://doi.org/10.1021/acsaem.0c00203>.

Heterojunction-composited architecture for Li–O₂ batteries with low overpotential and long-term cyclability.

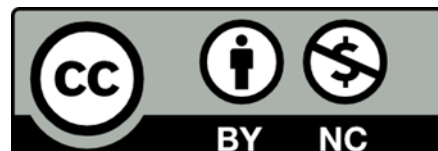
GE, B., WANG, J., SUN, Y., GUO, J., FERNANDEZ, C. and PENG, Q.

2020

This document is the Accepted Manuscript version of a Published Work that appeared in final form in ACS Applied Energy Materials, copyright © American Chemical Society after peer review and technical editing by the publisher. To access the final edited and published work see <https://doi.org/10.1021/acsaem.0c00203>.

 OpenAIR
@RGU

This document was downloaded from
<https://openair.rgu.ac.uk>



Heterojunction-Composited Architecture for Li–O₂ Batteries with Low Overpotential and Long-Term Cyclability

Bingcheng Ge, Jing Wang, Yong Sun, Jianxin Guo, Carlos Fernandez, and Qiuming Peng*

ABSTRACT: The crucial issue among lithium–oxygen batteries (LOBs) lies in the development of highly efficient catalysts to improve their large discharge–charge polarization, poor rate capability, and short cycle life. Herein, a composite of three-dimensional honeycomb graphene-supported a Mo/Mo₂C heterojunction has been synthesized and can be utilized as a self-supported LOB cathode directly. The LOBs based on the Mo/Mo₂C heterojunction composite cathode show a low overpotential of 0.52 V, a high discharge capacity of about 12016 mAh g^{−1} at 100 mA g^{−1}, and a long-term cyclability (about 360 cycles) under a restricted capacity of 1000 mAh g^{−1} at 100 mA g^{−1}, which exceeds the features of the majority of Mo-based catalysts for LOBs reported so far. Based on both experimental tests and density functional calculations, it is confirmed that the outstanding electrochemical performance is closely associated with a hierarchical porous structure for convenient oxygen/electrolyte diffusion, a large number of activity sites (interfaces/defects) for high capacity, and a high conductivity with metallic bonds for good rate capability. The method can be extended to prepare other metal based heterojunctions.

KEYWORDS: lithium–oxygen batteries, catalyst, overpotential, heterojunctions, Mo-based catalysts

1. INTRODUCTION

With the increasing consumption of fossil energy, both lithium ion and lithium–air batteries have been considered as green and renewable energy conversion and storage sources.^{1–5} Compared with lithium ion batteries, lithium–O₂ batteries (LOBs) possess a high energy density of ~3500 Wh kg^{−1} based on the reaction ($2\text{Li}^+ + \text{O}_2 + 2\text{e}^- \rightarrow \text{Li}_2\text{O}_2$, $E^0 = 2.96 \text{ V vs Li/Li}^+$) consisting of the oxygen reduction reaction (ORR) and oxygen evolution reaction (OER), which is 5–10 times higher than Li-ion batteries.^{6–10} Hence they have attracted extensive research enthusiasm recently. Nevertheless, a large number of technical challenges need to be overcome before industrial applications of LOBs, such as poor rate capability, low round trip efficiency, and poor cyclability. These problems are mainly related to the accumulation of discharge products (such as nonconductive Li₂O₂) in the cathode, which results in their poor reversibility, high polarization, and large overpotential when the discharge products are decomposed during charging.^{11,12} In this regard, the development of highly efficient cathode catalysts is a promising approach to improve life and reversibility of LOBs. Porous carbon materials have the advantages of a wide source of raw materials, good electrical conductivity, adjustable porous structure, and high specific volume.^{13–16} Therefore, they are popular choices for ORR and OER catalyst carriers for LOBs.^{17, 18}

However, the inert character of porous carbon materials gives rise to high discharge–charge overpotential for Li_2O_2 oxidation (~ 1 V).² Consequently, it is an urgent issue to improve cathode reaction kinetics for low overpotential and high energy efficiency. The common method is the development of composite cathodes by supporting catalysts such as noble metals, metal oxides, and metal carbides on carbon materials.^{19–21} Nevertheless, the scarcity and cost of noble metals and the poor conductivity of transition metal oxides greatly limit their practical applications. Comparatively, metal carbides are alternatives used as cathode catalysts for rechargeable LOBs due to their prominent electrocatalytic performances.²² Among transition metal carbides, Mo_2C is considered to be the most promising LOB electrodes because of its good electrochemical activity and low cost;^{23,24} however, the pure Mo_2C catalyst suffers from weak conductivity, limited activated sites, and poor structural stability. Subsequently, interface engineering efforts relative to a heterojunction have been attempted to enhance the electrochemical properties of Mo_2C catalysts.^{25,26} For example, a Mo_2N – Mo_2C hetero- junction is a high efficiency catalyst for hydrogen evolution.²⁶ The reaction center is located at Mo in the vicinity of the interface which modifies the local chemical environment of graphene oxide, exhibiting activity superior to Pt/C at large current densities (>88 mA cm^{-2}) in alkaline media. A MoC – Mo_2C heteronanowire²⁷ has been confirmed to be high activity in both acidic and basic solutions due to the optimized electron density created by the carbide surface. Additionally, hierarchical porous $\text{MoO}_2/\text{Mo}_2\text{C}$ heteronanotubes²⁸ have been developed as a promising anode material for high performance lithium-ion batteries. Unfortunately, owing to low conductivity, limited activated sites, and oxidation of these heterojunctions, some new and high performance Mo_2C heterojunctions are desirable for the accelerated rhythm of LOB applications. Herein, we prepared three-dimensional (3D) honeycomb graphene composites containing a $\text{Mo}/\text{Mo}_2\text{C}$ heterojunction by a convenient synthesis method. Depending on the geometry of the three-dimensional honeycomb structure, the interconnected honeycomb cells, and the $\text{Mo}/\text{Mo}_2\text{C}$ heterojunction structure, this self-supporting composite cathode delivers outstanding performances, achieving a low overpotential (0.52 V), a long cycle life (over 360 cycles), and a high specific capacity of 12016 mAh g^{-1} at a current density of 100 mA g^{-1} . Simultaneously, the catalytic mechanisms of composite electrodes were elucidated by microstructural observations, component identifications, and first-principles calculations in detail.

2. RESULTS AND DISCUSSION

2.1. Characteristics of the Mo/Mo₂C Heterojunction

Three-dimensional honeycomb graphenes and their composites were prepared by the following method. Typically, a Mg–5 wt % Mo alloy was prepared at 1200 °C for 30 min under a loading pressure of 4 GPa in a cubic-anvil large-volume press with six rams. And then, the alloys and pure magnesium were loaded into a ceramic tube reactor and exposed to CO with a flux of 60 mL min⁻¹ at different temperatures. Consequently, the reaction products were removed by acid cleaning and freeze-drying (the detailed procedure is described in the experimental procedure). As identified by X-ray diffraction (XRD, Figure 1a), the Mg–5 wt % Mo sample calcined at 800 °C is mainly composed of C, Mo, and Mo₂C peaks. Moreover, field-emission scanning electron microscopy (FESEM, Figure 1b–c) images show that the graphene sheets are curved and connected each other, resulting in the formation of a 3D honeycomb-like graphene structure (3DHG). This typical graphene character is also confirmed by Raman spectrum (Figure 1d). Similar structures have been also reported in Li₂O or Mg calcination.^{29,30} Subsequently, this unique structure has further been clarified by transmission electron microscopy (TEM Figure 1e). Four typical characters have been confirmed. First, a large number of fine particles with a diameter of about ~4.5 nm (calculated in terms of 50 random particles, Figure 1f) are homogeneously distributed on the graphene layers. Secondary, the high magnification atomic-scale image (Figure 1h) shows that the particle is related to a distinct heterojunction. One side is related to a hexagonal structure of Mo, as evidence by a spacing of ~0.22 nm. Comparatively, the other side is associated with the d-spacing of nanoparticle of 0.26 nm, which is ascribed to plane (100) of Mo₂C phase. Moreover, the 3DHG and 3DHG-Mo/Mo₂C heterojunction contents of the as-prepared 3DHG-Mo/Mo₂C-800 were further studied using thermogravimetric analysis (TGA) (Figure S1), in which 3DHG was determined to be 75.92% and Mo/Mo₂C heterojunction was determined to be 24.08%.³¹ The weight fraction of Mo/Mo₂C is about 2:1. This interpretation is also confirmed by selected area electron diffraction (SAED) pattern (Figure 1g) and XRD pattern (Figure 1a). Third, a large number of defects or vacancies are confirmed in both Mo and Mo₂C phases (white triangles, Figure 1h). Furthermore, the interface between Mo and Mo₂C is irregular, which is relative to the existence of interface stress owing to their mismatch lattices. Finally, the elemental mapping images (Figure 1i–k) show that both Mo and C elements are homogeneously distributed in the carbon layer. As a result, this unique 3D honeycomb graphene containing a Mo/Mo₂C heterojunction is denoted as 3DHG-Mo/Mo₂C-800.

In addition, the similar amorphous 3D honeycomb graphene (3DHG), evidenced by XRD, SEM, TEM, and Raman spectrum (Figure 1d and S2), has also been attained by calcining pure Mg under CO at 800 °C. This reference can be shown as 3DHG-800. Comparatively, when the calcined temperature of Mg–5 wt % Mo alloy is reduced to 700 °C, the thick honeycomb is attained, wherein some particles still remain (Figure S3). The HRTEM and atomic-scale image show that the nanoscale particles with the dimension of 2 nm are observed in the carbon layer. The lattice spacing of 0.217 nm demonstrates that these particles might be Mo, which is consistent with the XRD pattern (Figure 1a). Accordingly, the sample with a 3D honeycomb graphene and Mo particles can be defined as 3DHG-Mo-700. In turn, when the temperature is increased to 900 °C, both the fine 3DHG structure (160 nm) and pure Mo₂C precipitates have been achieved (Figure S4), as evidenced by the XRD result (Figure 1a). Notably, compared with 3DHG-Mo/Mo₂C-800, 3DHG structure becomes finer, but the dimensions of the Mo₂C precipitates change to be larger (over 10 nm). Hence, the Mg–5 wt % Mo sample after treatment at 900 °C can be marked as 3DHG-Mo₂C-900.

2.2. Electrochemical Properties in LOBs.

To investigate the electrochemical properties of all the hybrids, the samples and PVDF were mixed in a ratio of 9:1 and rolled as the cathodes to assemble into 2032-type batteries for electrochemical tests. The cyclic voltammetry (CV) curves under high pure O₂ (Figure 2a) was measured from 2 to 4.5 V versus Li/Li⁺ at a scan rate of 0.2 mV s⁻¹, which reveal that there are two peaks for both 3DHG-Mo/Mo₂C-800 and 3DHG-Mo₂C-900 cathodes, and they are totally different from the 3DHG-Mo-700 and 3DHG sample.³² Simultaneously, the ORR peaks of 3DHG-Mo/Mo₂C-800 are similar to those of 3DHG-Mo₂C-900. Notably, the onset potential of 3DHG-Mo/Mo₂C-800 is about 2.67 V, which is higher than that of 3DHG-Mo₂C-900 (about 2.65 V) and 3DHG-Mo-700 (2.44 V). Additionally, an obvious OER peak is also detected in both 3DHG-Mo/Mo₂C-800 and 3DHG-Mo₂C-900, but it is hardly distinguished in 3DHG-Mo-700.^{5,33} More importantly, compared with other two samples, 3DHG-Mo/Mo₂C-800 bestows a larger ORR/OER peak current. In brief, the above results demonstrate that 3DHG-Mo/Mo₂C-800 exhibits the highest ORR onset potential accompanying with the highest ORR/OER peak current, comparing with those of 3DHG-Mo₂C-900 and 3DHG-Mo-700. In this respect, 3DHG-Mo/Mo₂C-800 might be offer a potential higher ORR/OER activity toward both the decomposition of discharge product in LOBs.

The galvanostatic discharge/charge profiles of four composites were carried out within the voltage range from 2 to 4.4 V at a current density of 100 mA g⁻¹ (Figure 2b). The 3DHG-Mo/Mo₂C-800 cathode delivers a discharge capacity of about 12016 mAh g⁻¹ and charge capacity of 11602 mAh g⁻¹, which are higher than those of 3DHG-800, 3DHG-Mo-700, and 3DHG-Mo₂C-900 electrodes (Figures S5, S7, and S8), consequently yielding a high roundtrip efficiency of about 96.5% in the deep discharge-charge model. In addition, when the discharge/charge capacity is limited to 1000 mAh g⁻¹ at a density of 100 mA g⁻¹ (Figure 2c), the 3DHG-Mo/Mo₂C-800 cathode shows low polarization, as evidenced by a discharge-charge overpotential of 0.52 V. In contrast, the overpotential values increase to 0.93 V for 3DHG-800, 0.76 V for 3DHG-Mo-700, and 0.82 V for 3DHG-Mo₂C-900, respectively. Attractively, this value for 3DHG-Mo/Mo₂C-800 is merely about 39.4% of commercial KB (1.32 V) (Figure S5). It shows that the 3DHG-Mo/Mo₂C-800 cathode offers outstanding catalytic activity.

To confirm the absolute recovery of discharge products and ameliorate the ORR/OER of LOBs, we examined the batteries with a limited depth of discharge-charge under high pure O₂. 3DHG-Mo/Mo₂C-800 operates for 360 cycles, when the cutoff capacity of LOBs is limited at 1000 mAh g⁻¹ at the current density of 100 mA g⁻¹ (Figure 2d). Even at a high current density of 300 mA g⁻¹ (Figure S6a-b), the battery with 3DHG-Mo/Mo₂C-800 cathode can also run well for more than 160 cycles. By comparison, the cycling numbers change to 190 cycles for 3DHG-Mo-700 and 210 cycles for 3DHG-Mo₂C-900 under the 100 mA g⁻¹ current density, respectively (Figures S7-S8). Moreover, with an increase in the current density to 300 mA g⁻¹, these cycling values are further reduced to 120 cycles for 3DHG-Mo-700 and 150 cycles for 3DHG-Mo₂C-900, respectively. Note that the cycling performances are poor for both commercial KB and 3DHG-800, wherein their numbers are no more than 50 cycles in the range of 100-300 mA g⁻¹ current density (Figure S5). Figure 2e illustrates the terminal potentials as a function of cycle number at various current rates. Basically, the polarization of the system becomes serious when the current density increased, as this phenomenon is commonly observed in LOBs.^{34,35}

To probe the current rate performances, the LOBs composed of different composites were studied with a fixed capacity of 1000 mA h g⁻¹. Figure 2f shows the voltage versus cycle number on the discharge-charge terminal of the LOBs with four different cathodes at 100 mA g⁻¹. Noteworthy, the battery with the cathode with 3DHG-Mo/Mo₂C-800 exhibits superior current rate performances (360 cycles). To better illustrate the superiority of the 3DHG-Mo/Mo₂C-800 cathode, a comparison between the cycling performances and overpotential of our cathode and

those main Mo–C cathodes reported so far are presented in [Figure 2g,23,24,28,32,36–39](#) wherein the 3DHG-Mo/Mo₂C-800 cathode has the longest cycle life (~360 cycles) accompanied with a very low overpotential (~0.52 V).

2.3. Reaction Processes.

[Figure 3a](#) shows the initial galvanostatic discharge–charge curve of the LOBs with the 3DHG-Mo/Mo₂C-800 cathode at the current density of 100 mA g⁻¹. XRD patterns ([Figure 3b](#)) show that some new diffraction peaks can be seen at 32.9°, 35.0°, 47.2°, and 48.9°, which are in perfect agreement with the standard pattern of Li₂O₂ (JCPDS no. 09-0355). This is also confirmed by the Raman spectrum (~787 cm⁻¹, [Figure 3c](#)) and galvanostatic intermittent titration technique (GITT) testing (2.96 V, [Figure S6c](#)).⁴⁰ After charging, Li₂O₂ completely disappeared. This reaction process has also been identified by ex-situ SEM observations. After discharging from position A to position B, some nanosheet-shaped Li₂O₂ discharge products are observed ([Figure 3d–e](#)). Note that this hierarchical porous structure and nanosheet structure reveal that oxygen and electrolyte are evenly distributed around the discharge products and promote the decomposition of Li₂O₂ products during the charging process ([Figure 3f](#)). More importantly, the similar morphology of the 3DHG-Mo/Mo₂C-800 electrode remains well after 100 cycles ([Figure S9](#)), revealing the good reversibility of Li₂O₂ products. On the contrary, owing to the low catalytic activity, the reaction discharged products cannot decompose absolutely for the other three samples ([Figure S10](#)), which cover the surfaces of the electrodes, resulting in their weak cyclability. In-situ environmental TEM has further been applied to observe the morphology and structure evolution of 3DHG-Mo/Mo₂C-800 during the discharge–charge process.^{41,42} The images in [Figure 4a–c](#) (captured from [Movie 1](#)) show the morphological variation of the 3DHG-Mo/Mo₂C-800 cathode in different states. With the increment of the discharge time, Li₂O₂ gradually grows and increases, and the surface of the 3DHG-Mo/Mo₂C-800 electrode becomes coarse. Conversely, as the charging process proceeds, the product gradually disappeared, until the electrode surface is as clean as that of the pristine electrode. The in-situ SAED patterns ([Figure 4d–f](#)) show that the primitive electrode is composed of C, Mo, and Mo₂C. This changes to a mixture of C, Mo, Mo₂C, and Li₂O₂ after discharging, and then, the nanowire returns to being C, Mo, and Mo₂C. These results are also verified by the electron energy loss spectroscopy (EELS) analysis ([Figure 4g–h](#)), in which the appearance/disappearance of the Li₂O₂ peaks (59.3, 64.5, and 67.5 eV) shows no structural change during the reactive process and also indicates the high reversibility of the battery with the 3DHG-Mo/Mo₂C-800 electrode.

2.4. Catalytic Mechanism of Heterojunction.

To elucidate the high electrochemical properties of 3DHG-Mo/Mo₂C-800 electrode, X-ray photoelectron spectroscopy (XPS) tests have been performed to analyze the valence variation of the electrode at different discharge/charge stages. As shown in [Figure 5a](#), the peak fitting result suggests that there are five valence states for Mo (Mo⁰, Mo²⁺, Mo³⁺, Mo⁴⁺, and Mo⁶⁺), and the fitting fractions are summarized in [Table S1](#). The Mo⁰ might be related to elementary Mo, and the low oxidation states of Mo²⁺ and Mo³⁺ may be due to Mo–C bonds in Mo₂C. In contrast, the existence of Mo⁴⁺ and Mo⁶⁺ may be due to the formation of MoO₂ and MoO₃ when the sample is exposed to the air.^{31,43,44} After cycling ([Figure 5b–c](#)), the fractions of the Mo⁰ state decrease sharply, while the fractions of Mo²⁺ and Mo³⁺ remain stable. Note that the amount of Mo⁴⁺ and Mo⁶⁺ is increased after cycling, which might be related to the formation of oxides owing to the oxidation of Mo. Consequently, the oxidation of Mo⁰ will remarkably reduce the concentration of O, and then, the oxidation of Mo₂C will be prohibited correspondingly. Additionally, the appearance/disappearance of Li 1s peak ([Figure 5d–f](#)) reveals that the formation and decomposition of Li₂O₂ is reversible.

In addition, the electrochemical properties of the 3DHG-Mo/ Mo₂C-800 electrode are also related to the specific surface area and pore-size distribution. 3DHG-Mo-700, 3DHG-Mo/ Mo₂C-800, and 3DHG-Mo₂C-900 composites show similar surface areas of ~96.8 m² g⁻¹ (Figure S11a), which is lower than those of 3DHG-800 (~155.8 m² g⁻¹). However, note that both fine pores (~2.2 nm) and coarse pores (~20 nm) (Figure S11b) are detected in the 3DHG-Mo/Mo₂C-800 sample. This hierarchical structure in pore distribution, especial wide pore dimension, accelerates ion transformation, improving both capacity and rate performance.⁴⁵ This trend is also confirmed by EIS measure (Figure S12), in which the lowest charge transfer resistance accounts for the highest conductivity.⁴⁶ Moreover, the overlapped curves indicate its high reversibility. To probe the underlying mechanism on the outstanding catalytic activity of the Mo/Mo₂C heterojunction, density functional calculations have been conducted. As shown in Figure 6a, it is obvious that charge redistribution occurs in the vicinity of the heterojunction interface, which is beneficial to improving electron mobility and thus catalytic activity. Moreover, the electronic local function (ELF) shown in Figure 6b–d gives rise to the electronic local distribution related to the interfaces, i.e., P1, P2, and P3 as indicated. This reveals that the ELF in the position of P1, which is dominated by Mo 3d electrons, behaves as an electron gas (green color, ELF = 0.5) and shows metallic character. As far as the Mo₂C (as in P3) is concerned, the electron in the neighborhood of C is highly localized (surrounded by red with ELF = 0.9) and Mo acts as an electron donator, indicating that it is typically ionically bound (Mo–C). By contrast, electrons at the interface (P2) are highly delocalized, reflected by the blue color in between atoms with ELFs around 0.2. More importantly, as shown in Figure 6e, differing from that in Mo₂C, an upshift of the d band center to the Fermi level is achieved in the Mo/Mo₂C interface, indicating the stronger O₂ binding energy. Simultaneously, a larger DOS value in the Fermi level of Mo/Mo₂C interface might be associated with more electrons for conductivity in contrast to Mo₂C, resulting in a higher rate performance.

3. CONCLUSIONS

In summary, a 3DHG-Mo/Mo₂C heterojunction composite electrode was prepared using a facile solid-phase synthesis. On the one hand, the three-dimensional honeycomb structure with interconnected walls and cells can provide sufficient channels for achieving rapid electron transfer and Li-ion and oxygen diffusion, which offers excellent reaction kinetics. On the other hand, the unique Mo/Mo₂C heterojunction provides an enhanced conductivity, plenty of activated sites, and the reduction of Mo₂C oxidation, resulting in excellent electrocatalytic performance. Typically, the LOBs using 3DHG-Mo/Mo₂C-800 as the cathode have a low overpotential (0.52 V), which can be run well over 360 cycles under the conditions of current density of 100 mA g⁻¹ and limited capacity of 1000 mAh g⁻¹. In particular, this technique can be extended to prepare other 3D honeycomb metal–metal carbon heterojunctions, which undoubtedly inspires future wide applications of these heterojunctions such as those in biomedical, chemical, and material sciences.

■ ACKNOWLEDGMENTS

We greatly acknowledge the financial support from National Natural Science Foundation-Outstanding Youth Foundation (51771162, 51971194) and Hebei Province Talent project (A201910002). We would like to express our gratitude to Hebei Province Youth Top-notch Talent Program and the High Performance Computing Platform of Hebei University.

FIGURES

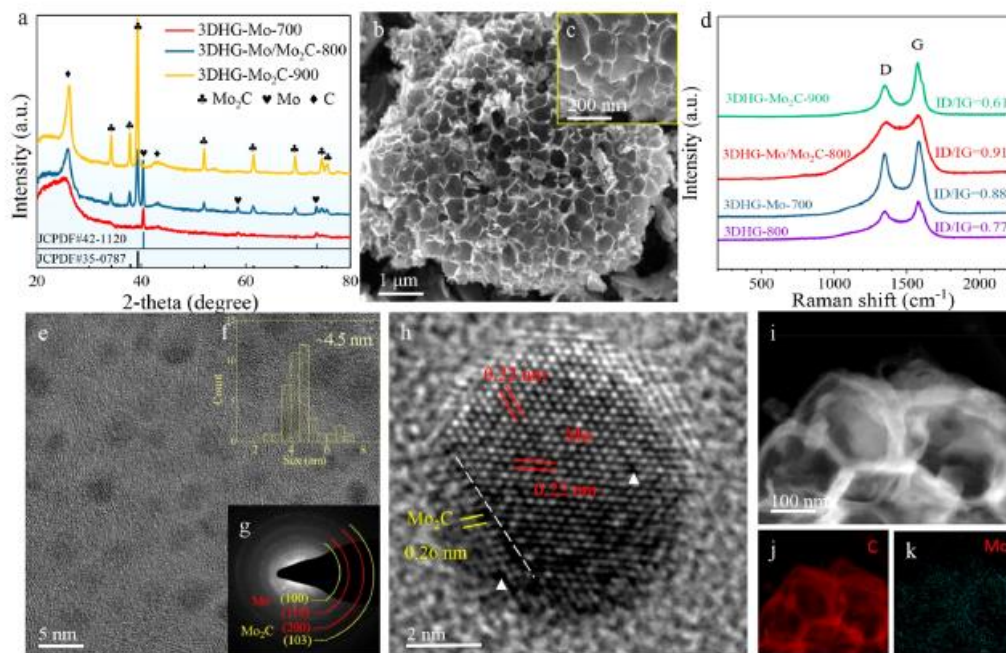


Figure 1. Structural characteristics. (a) XRD patterns of different composites. (b and c) SEM images of 3DHG-Mo/Mo₂C-800. (d) Raman spectra of the different samples. ID/IG is the intensity ratio of D- and G-peaks, and I here represents the intensity ratio. (e) TEM image of 3DHG-Mo/Mo₂C-800. (f and g) Size distribution and SAED pattern of the Mo/Mo₂C nanoparticles. (h) HAADF-STEM image of the Mo/Mo₂C heterojunction. TEM image (i) and EDX element mapping images (j–k) of 3DHG-Mo/Mo₂C-800.

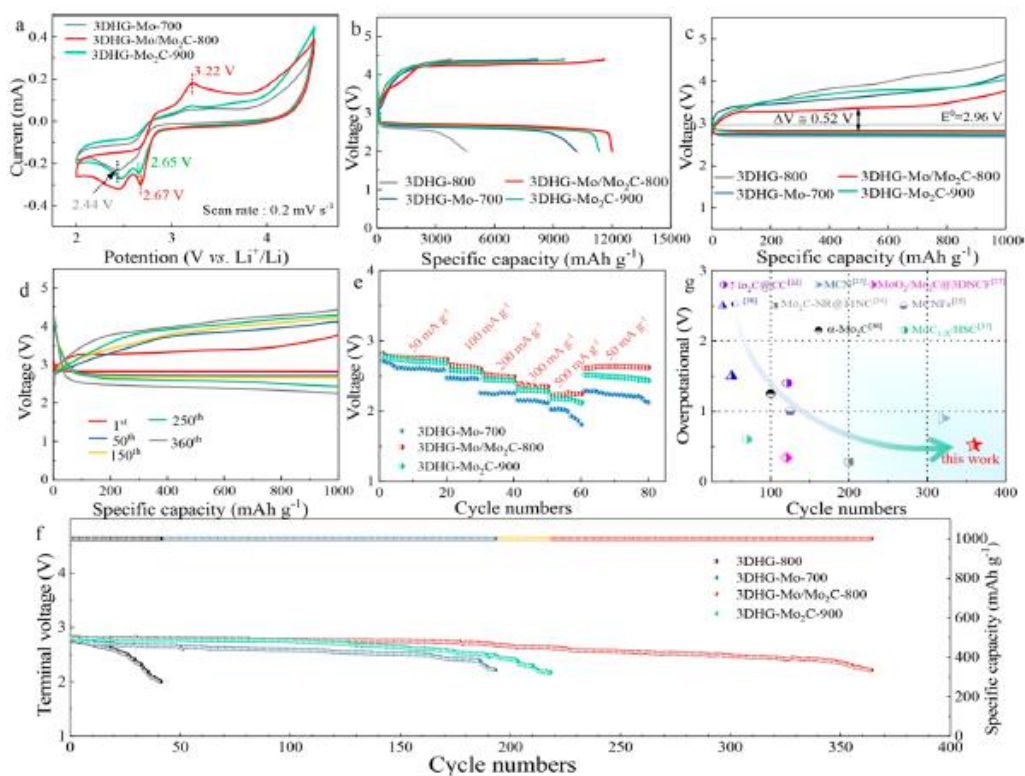


Figure 2. Electrochemical properties of LOBs with 3DHG-800, 3DHG-Mo-700, 3DHG-Mo/Mo₂C-800, and 3DHG-Mo₂C-900 electrodes. (a) CV curves from 2.0 to 4.5 V (vs Li⁺/Li) under a scan rate of 0.2 mV s⁻¹. (b) Initial fully discharge-charge profiles at a current density of 100 mA g⁻¹. (c) First discharge-charge cycle of the LOBs with five different cathodes at a current density of 100 mA g⁻¹. (d) Discharge-charge cycling stability of the 3DHG-Mo/Mo₂C-800 electrode at 100 mA g⁻¹ with a cutoff capacity of 1000 mAh g⁻¹. (e) Terminal voltages as a function of cycle number at various current densities of different samples. (f) Cycling stability and terminal discharge-charge voltages of 3DHG-Mo/Mo₂C-800 cathode at 100 mA g⁻¹ with a limited capacity of 1000 mAh g⁻¹. (g) Comparison of the electrochemical performances of the 3DHG-Mo/Mo₂C-800 cathode with those of other reported Mo-C based LOBs.

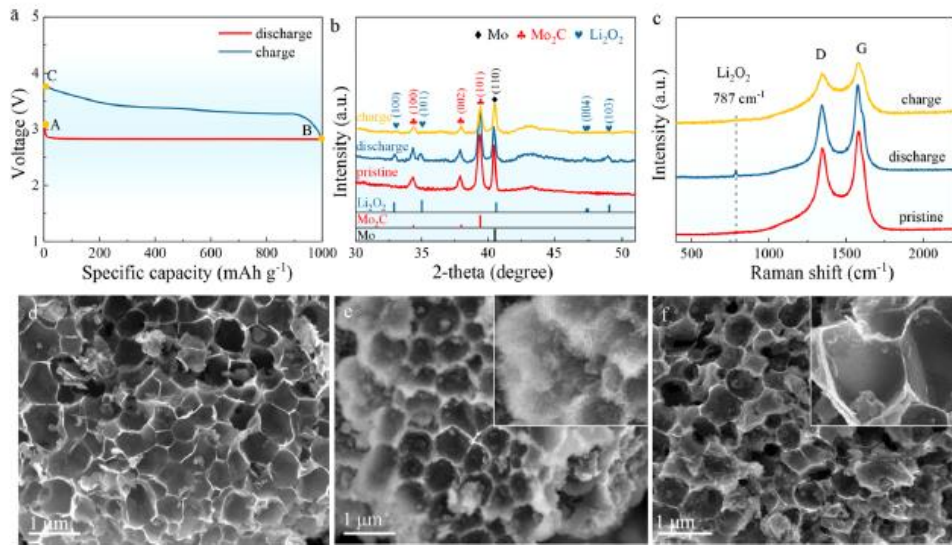


Figure 3. Characteristics of the discharged/charged products. (a) Initial cycle galvanostatic discharge–charge profiles. (b) Ex-situ XRD patterns of discharged samples corresponding to the different positions in part a. (c) Raman spectra of the different states of 3DHG Mo/Mo₂C-800. Typical SEM images of 3DHG-Mo/Mo₂C-800 with the pristine (d), discharged (e), and charged (f) states, respectively. (insets) Local high magnification images.

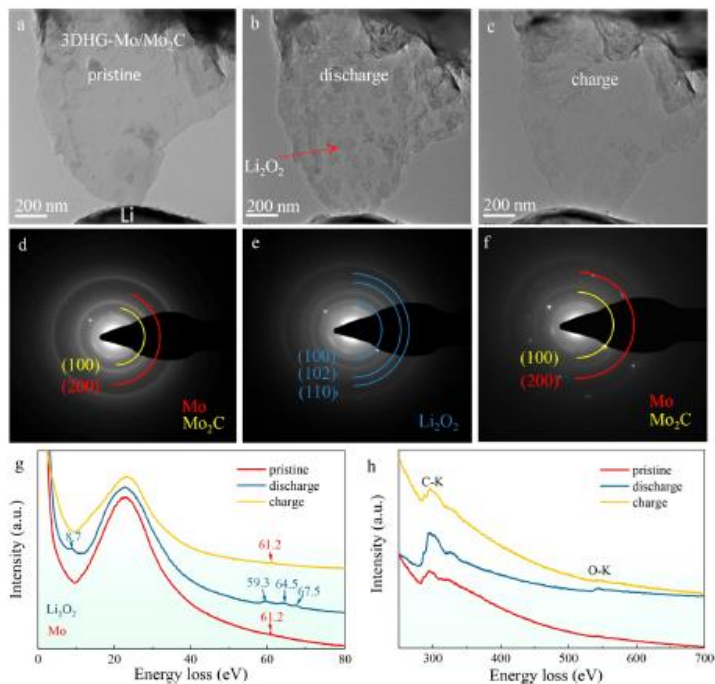


Figure 4. In-situ microstructural features of 3DHG-Mo/Mo₂C-800. Typical morphology variation during the discharged process from a to b and the charged process b to c. In-situ SAED patterns of the primitive (d), discharged (e), and charged (f) states. (g and h) Low-loss and core-loss EELS of 3DHG-Mo/Mo₂C-800 electrode at different states.

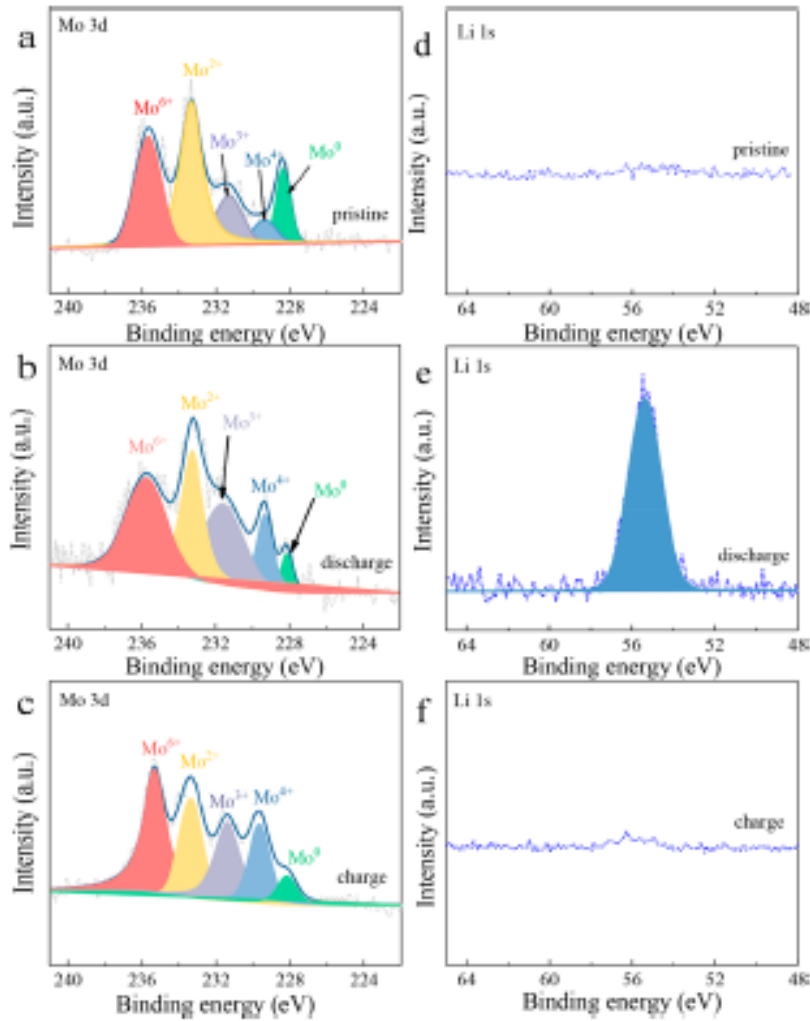


Figure 5. XPS spectra variation. Ex-situ high resolution XPS spectra of Mo 3d (a–c) and Li 1s (d–f) at different discharge–charge statuses of 3DHG-Mo/Mo₂C-800 for the first cycle.

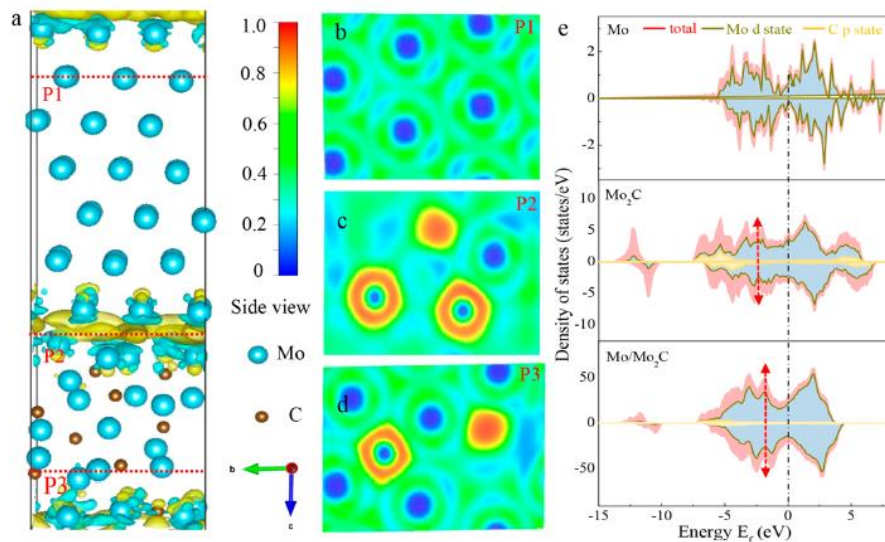
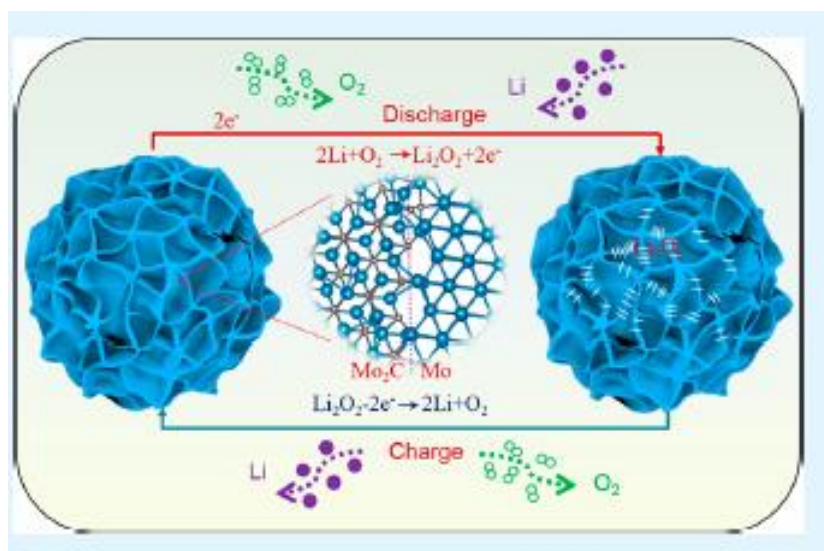


Figure 6. Theoretical calculations. (a) Schematic model of the lattice matching and distribution of charge density difference at Mo (110) and Mo₂C (100) interface. (b–d) ELF maps of different surfaces of the heterojunction. (e) Atom-projected DOS for Mo, Mo₂C, and Mo/Mo₂C heterojunction.

GRAPHICAL ABSTRACT



■ REFERENCES

- (1) Aurbach, D.; McCloskey, B. D.; Nazar, L. F.; Bruce, P. G. Advances in understanding mechanisms underpinning lithium–air batteries. *Nature Energy* 2016, 1, 16128.
- (2) Jung, K.-N.; Kim, J.; Yamauchi, Y.; Park, M.-S.; Lee, J.-W.; Kim, J. H. Rechargeable lithium–air batteries: A perspective on the development of oxygen electrodes. *J. Mater. Chem. A* 2016, 4, 14050–14068.
- (3) Liu, T.; Xu, J.; Liu, Q.; Chang, Z.; Yin, Y.; Yang, X.; Zhang, X. Ultrathin, lightweight, and wearable Li-O₂ battery with high robustness and gravimetric/volumetric energy density. *Small* 2017, 13, 1602952.

- (4) Yang, X.; Xu, J.; Bao, D.; Chang, Z.; Liu, D.; Zhang, Y.; Zhang, X. High-performance integrated self-package flexible Li–O₂ battery based on stable composite anode and flexible gas diffusion layer. *Adv. Mater.* 2017, 29, 1700378.
- (5) Yang, X.; Xu, J.; Bao, D.; Chang, Z.; Liu, D.; Zhang, Y.; Zhang, X. High-performance integrated self-package flexible Li–O₂ battery based on stable composite anode and flexible gas diffusion layer. *Adv. Mater.* 2017, 29, 1700378.
- (6) Bruce, P. G.; Freunberger, S. A.; Hardwick, L. J.; Tarascon, J.-M. Li–O₂ and Li–S batteries with high energy storage. *Nat. Mater.* 2012, 11, 19–29.
- (7) Qiao, Y.; Yi, J.; Guo, S.; Sun, Y.; Wu, S.; Liu, X.; Yang, S.; He, P.; Zhou, H. Li₂CO₃-free Li–O₂/CO₂ battery with peroxide discharge product. *Energy Environ. Sci.* 2018, 11, 1211–1217.
- (8) Ottakam Thotiyl, M. M.; Freunberger, S. A.; Peng, Z.; Chen, Y.; Liu, Z.; Bruce, P. G. A stable cathode for the aprotic Li–O₂ battery. *Nat. Mater.* 2013, 12, 1050–1056.
- (9) Xia, C.; Kwok, C. Y.; Nazar, L. F. A high-energy-density lithiumoxygen battery based on a reversible four-electron conversion to lithium oxide. *Science* 2018, 361, 777–781.
- (10) Liu, B.; Sun, Y.; Liu, L.; Xu, S.; Yan, X. Advances in manganesebased oxides cathodic electrocatalysts for Li–air batteries. *Adv. Funct. Mater.* 2018, 28, 1704973.
- (11) Asadi, M.; Sayahpour, B.; Abbasi, P.; Ngo, A. T.; Karis, K.; Jokisaari, J. R.; Liu, C.; Narayanan, B.; Gerard, M.; Yasaei, P.; Hu, X.; Mukherjee, A.; Lau, K. C.; Assary, R. S.; Khalili-Araghi, F.; Klie, R. F.; Curtiss, L. A.; Salehi-Khojin, A. A lithium–oxygen battery with a long cycle life in an air-like atmosphere. *Nature* 2018, 555, 502–506.
- (12) Xin, X.; Ito, K.; Dutta, A.; Kubo, Y. Dendrite-Free Epitaxial Growth of Lithium Metal during Charging in Li–O₂ Batteries. *Angew. Chem.* 2018, 130, 13390–13394.
- (13) Hou, H.; Banks, C. E.; Jing, M.; Zhang, Y.; Ji, X. Carbon quantum dots and their derivative 3D porous carbon frameworks for sodium-ion batteries with ultralong cycle life. *Adv. Mater.* 2015, 27, 7861–7866.
- (14) Liu, H.; Li, W.; Shen, D.; Zhao, D.; Wang, G. Graphitic carbon conformal coating of mesoporous TiO₂ hollow spheres for highperformance lithium ion battery anodes. *J. Am. Chem. Soc.* 2015, 137, 13161–13166.
- (15) Schuster, J.; He, G.; Mandlmeier, B.; Yim, T.; Lee, K. T.; Bein, T.; Nazar, L. F. Spherical ordered mesoporous carbon nanoparticles with high porosity for lithium-sulfur batteries. *Angew. Chem., Int. Ed.* 2012, 51, 3591–3595.
- (16) Tan, G.; Chong, L.; Amine, R.; Lu, J.; Liu, C.; Yuan, Y.; Wen, J.; He, K.; Bi, X.; Guo, Y.; Wang, H.-H.; Shahbazian-Yassar, R.; Al Hallaj, S.; Miller, D. J.; Liu, D.; Amine, K. Toward highly efficient electrocatalyst for Li–O₂ batteries using biphasic N-doping cobalt@ graphene multiplecapsule heterostructures. *Nano Lett.* 2017, 17, 2959–2966.
- (17) Meng, X. K.; Liao, K. M.; Dai, J.; Zou, X. H.; She, S. X.; Zhou, W.; Ye, F.; Shao, Z. P. Ultralong Cycle Life Li–O₂ Battery Enabled by a MOF-Derived Ruthenium–Carbon Composite Catalyst with a Durable Regenerative Surface. *ACS Appl. Mater. Interfaces* 2019, 11, 20091–20097.

- (18) Wang, G.; Tu, F.; Xie, J.; Du, G.; Zhang, S.; Cao, G.; Zhao, X. High-performance Li–O₂ batteries with controlled Li₂O₂ growth in graphene/Au-nanoparticles /Au-nanosheets sandwich. *Adv. Sci.* 2016, 3, 1500339.
- (19) Jung, H.-G.; Jeong, Y. S.; Park, J.-B.; Sun, Y.-K.; Scrosati, B.; Lee, Y. J. Ruthenium-based electrocatalysts supported on reduced graphene oxide for lithium-air batteries. *ACS Nano* 2013, 7, 3532–3539.
- (20) Li, F.; Chen, Y.; Tang, D.-M.; Jian, Z.; Liu, C.; Golberg, D.; Yamada, A.; Zhou, H. Performance-improved Li–O₂ battery with Ru nanoparticles supported on binder-free multi-walled carbon nanotube paper as cathode. *Energy Environ. Sci.* 2014, 7, 1648–1652.
- (21) Sun, B.; Munroe, P.; Wang, G. Ruthenium nanocrystals as cathode catalysts for lithium-oxygen batteries with a superior performance. *Sci. Rep.* 2013, 3, 2247.
- (22) Oshikawa, K.; Nagai, M.; Omi, S. Characterization of molybdenum carbides for methane reforming by TPR, XRD, and XPS. *J. Phys. Chem. B* 2001, 105, 9124–9131.
- (23) Luo, Y.; Jin, C.; Wang, Z.; Wei, M.; Yang, C.; Yang, R.; Chen, Y.; Liu, M. A high-performance oxygen electrode for Li–O₂ batteries: Mo₂C nanoparticles grown on carbon fibers. *J. Mater. Chem. A* 2017, 5, 5690–5695.
- (24) Zhu, Q. C.; Xu, S. M.; Harris, M. M.; Ma, C.; Liu, Y. S.; Wei, X.; Xu, H. S.; Zhou, Y. X.; Cao, Y. C.; Wang, K. X.; Chen, J. S. A composite of carbon-wrapped Mo₂C nanoparticle and carbon nanotube formed directly on Ni foam as a high-performance binder-free cathode for Li–O₂ batteries. *Adv. Funct. Mater.* 2016, 26, 8514–8520.
- (25) Dong, J.; Wu, Q.; Huang, C.; Yao, W.; Xu, Q. Cost effective Mo rich Mo₂C electrocatalysts for the hydrogen evolution reaction. *J. Mater. Chem. A* 2018, 6, 10028–10035.
- (26) Yan, H. J.; Xie, Y.; Jiao, Y. Q.; Wu, A. P.; Tian, C. G.; Zhang, X. M.; Wang, L.; Fu, H. G. Holey reduced graphene oxide coupled with an Mo₂N–Mo₂C heterojunction for efficient hydrogen evolution. *Adv. Mater.* 2018, 30, 1704156.
- (27) Xiong, J.; Li, J.; Shi, J. W.; Zhang, X. L.; Suen, N. T.; Liu, Z.; Huang, Y. J.; Xu, G. X.; Cai, W. W.; Lei, X. R.; et al. In Situ Engineering of Double-Phase Interface in Mo/Mo₂C Heteronanoshells for Boosted Hydrogen Evolution Reaction. *ACS Energy Lett.* 2018, 3, 341.
- (28) Lu, Y.; Ang, H.; Yan, Q.; Fong, E. Bioinspired synthesis of hierarchically porous MoO₂/Mo₂C nanocrystal decorated N-doped carbon foam for lithium–oxygen batteries. *Chem. Mater.* 2016, 28, 5743–5752.
- (29) Wang, H.; Sun, K.; Tao, F.; Stacchiola, D. J.; Hu, Y. H. 3D honeycomb-like structured graphene and its high efficiency as a counter-electrode catalyst for dye-sensitized solar cells. *Angew. Chem., Int. Ed.* 2013, 52, 9210–9214.
- (30) Hu, X.; Li, Z.; Zhao, Y.; Sun, J.; Zhao, Q.; Wang, J.; Tao, Z.; Chen, J. Quasi–solid state rechargeable Na–CO₂ batteries with reduced graphene oxide Na anodes. *Sci. Adv.* 2017, 3, e1602396.
- (31) Hou, Y.; Wang, J.; Liu, L.; Liu, Y.; Chou, S.; Shi, D.; Liu, H.; Wu, Y.; Zhang, W.; Chen, J. Mo₂C/CNT: An efficient catalyst for rechargeable Li–CO₂ batteries. *Adv. Funct. Mater.* 2017, 27, 1700564.

- (32) Jung, I.-S.; Kwon, H. J.; Kim, M.; Kim, D.; Kim, J.-H.; Lee, H.; Yun, D.; Byun, S.; Yu, D.; An, H.; Jang, J.; Im, D.; Lee, H. Rapid oxygen diffusive lithium–oxygen batteries using a restacking-inhibited, free-standing graphene cathode film. *J. Mater. Chem. A* 2019, 7, 10397–10404.
- (33) Yoon, K. R.; Shin, K.; Park, J.; Cho, S. H.; Kim, C.; Jung, J. W.; Cheong, J. Y.; Byon, H. R.; Lee, H. M.; Kim, I. D. Brush-like cobalt nitride anchored carbon nanofiber membrane: current collector/catalyst integrated cathode for long cycle Li–O₂ batteries. *ACS Nano* 2018, 12, 128–139.
- (34) Li, F.; Tang, D. M.; Chen, Y.; Golberg, D.; Kitaura, H.; Zhang, T.; Yamada, A.; Zhou, H. Ru/ITO: A carbon-free cathode for nonaqueous Li–O₂ battery. *Nano Lett.* 2013, 13, 4702–4707.
- (35) Liu, Q. C.; Xu, J.; Xu, D.; Zhang, X. Flexible lithium–oxygen battery based on a recoverable cathode. *Nat. Commun.* 2015, 6, 7892.
- (36) Sun, G.; Zhao, Q.; Wu, T.; Lu, W.; Bao, M.; Sun, L.; Xie, H.; Liu, J. 3D foam-like composites of Mo₂C nanorods coated by Ndoped carbon: a novel self-standing and binder-free O₂ electrode for Li–O₂ batteries. *ACS Appl. Mater. Interfaces* 2018, 10, 6327–6335.
- (37) Yang, Z. D.; Chang, Z. W.; Zhang, Q.; Huang, K.; Zhang, X. B. Decorating carbon nanofibers with Mo₂C nanoparticles towards hierarchically porous and highly catalytic cathode for high-performance Li–O₂ batteries. *Sci. Bull.* 2018, 63, 433–440.
- (38) Yu, H.; Dinh, K. N.; Sun, Y.; Fan, H.; Wang, Y.; Jing, Y.; Li, S.; Srinivasan, M.; Yan, Q. Performance-improved Li–O₂ batteries by tailoring the phases of Mo_xC porous nanorods as an efficient cathode. *Nanoscale* 2018, 10, 14877–14884.
- (39) Xing, Y.; Yang, Y.; Chen, R.; Luo, M.; Chen, N.; Ye, Y.; Qian, J.; Li, L.; Wu, F.; Guo, S. Strongly coupled carbon nanosheets/molybdenum carbide nanocluster hollow nanospheres for high performance aprotic Li–O₂ battery. *Small* 2018, 14, 1704366.
- (40) Lim, H.-K.; Lim, H.-D.; Park, K.-Y.; Seo, D.-H.; Gwon, H.; Hong, J.; Goddard, W. A.; Kim, H.; Kang, K. Toward a lithium–“air” battery: the effect of CO₂ on the chemistry of a lithium–oxygen cell. *J. Am. Chem. Soc.* 2013, 135, 9733–9742.
- (41) Liu, Q.; Yang, T.; Du, C.; Tang, Y.; Sun, Y.; Jia, P.; Chen, J.; Ye, H.; Shen, T.; Peng, Q.; Zhang, L.; Huang, J. In situ imaging the oxygen reduction reactions of solid state Na–O₂ batteries with CuO nanowires as the air cathode. *Nano Lett.* 2018, 18, 3723–3730.
- (42) Ge, B.; Sun, Y.; Guo, J.; Yan, X.; Fernandez, C.; Peng, Q. A Codoped MnO₂ catalyst for Li–CO₂ batteries with low overpotential and ultrahigh cyclability. *Small* 2019, 15, 1902220.

Supporting Information

A Heterojunction-Composited Architecture for Li-O₂ Batteries with Low Overpotential and Long-Term Cyclability

*Bingcheng Ge, Jing Wang, Yong Sun, Jianxin Guo, Carlos Fernandez, Qiuming Peng**

Dr. Bingcheng Ge, Jing Wang, Yong Sun, Prof. Qiuming Peng

State Key Laboratory of Metastable Materials Science and Technology, Yanshan University,

Qinhuangdao 066004, China

E-mail: pengqiuming@gmail.com

Dr. Jianxin Guo,

Hebei Provincial Key Lab of Optoelectronic Information Materials, College of Physics

Science and Technology, Hebei University, Baoding, 071002, China.

Dr. Carlos Fernandez

School of Pharmacy and life sciences, Rober Gordon University, Aberdeen, AB107GJ,

United Kingdom

Experimental Sections

Synthesis of heterojunctions

Mg-5wt.% Mo precursors has been prepared by ultrahigh melting method. Specifically, the powders were wrapped with Ta foil and then inserted into a BN crucible in a cubic-anvil large-volume press with six rams. The loading pressure (4 GPa) was added before increasing the temperature. The temperatures varied from room temperature to 1200 °C. The time was 30 min. After ultrahigh pressure treatment, the samples were quenched to room temperature. Subsequently, the alloy was loaded into a ceramic tube reactor and exposed to CO at a flux of 60 ml min⁻¹. The reaction temperatures were 700 °C, 800 °C and 900 °C, respectively. The reactor temperature was increased from room temperature to high temperature at a rate of 5 °C min⁻¹ and then kept for a 5 h, followed by cooling down to room temperature. These products were treated by 10 wt% hydrochloric acid (HCl) and washed with de-ionized water until the pH of around 7. The residual solids were separated from water by centrifugation (8000 rpm) and then freeze dried for 24 h to get the powders. Finally, the sample which treated at 700 °C was mainly composed of 3D honeycomb graphene (3DHG) and Mo particles (denoted as 3DHG-Mo-700). In contrast, the samples at 800 °C and 900 °C were involved Mo/Mo₂C and Mo₂C except for 3DHG, respectively. They were remarked as 3DHG-Mo/Mo₂C-800 and 3DHG-Mo₂C-900 correspondingly. The pure Mg sample treated at 800 °C was introduced as reference (3DHG-800).

Structural Characterization

Powder X-ray diffraction (XRD) patterns were collected on an X-ray diffraction (Rigaku D/MAX-2005/PC) using a filtered Cu K_α radiation at a sweep rate of 2 degree/min, Scanning electron microscope (SEM) was characterized by Hitachi S-4800. Transmission electron microscope (TEM) images, electron energy loss spectrum (EELS) analysis and elemental mapping were observed on a Titan ETEM G2 at 300 kV. The specific surface areas and pore size distribution were measured by a Micromeritics ASAP2020 using nitrogen gas adsorption at 77 K (-196 °C). X-ray photoelectron spectroscopy (XPS) patterns were conducted on a ThermoFisher with Al K_α (1486.71 eV) X-ray radiation (15 kV and 10 mA). The binding energies obtained in the XPS analysis were corrected by referencing the C 1s peak position

(284.60 eV). Raman spectroscopy was obtained from Renishaw micro-Raman spectroscopy with a laser radiation of 514 nm.

Li-O₂ battery assembly

The Li-O₂ battery assembly was performed based on a CR2032 coin type battery. It was successively assembled by stacking a lithium metal anode (14 mm in diameter), a piece of glass fiber separator (16 mm in diameter, Whatman) soaked with 80 μ L of electrolyte (1 M LiTFSI dissolved in TEGDME solution) and a rolled cathode with slurry (90 wt% of active material and 10 wt% polyvinylidene fluoride in methyl-2-pyrrolidone). The cathodes were cut into disks. Several holes (4 mm in diameter) were drilled in the cathode shell so that the O₂ can easily and quickly access the cathode. Then, the assembled batteries were placed in a 250 mL glass vessel filled with high-purity O₂. The pure O₂ was pumped into the glass vessel through the straight two-way piston conducted alternatively by vacuuming and ventilating for three times. After incubating for 10 h, the discharge and charge cycles of the batteries were tested. All potentials were referenced against Li/Li⁺.

Electrochemical test

The galvanostatic discharge/charge tests were collected on a LAND CT2001A battery test instrument. The specific capacity and current density were calculated according to the mass of active material on the electrodes. The mass loading of active material (3DHG) on carbon paper was found to be 0.3-0.5 mg cm⁻². Cyclic voltammetry (CV) curves were conducted on a BioLogic VMP3 electrochemical workstation in the potential window of 2.0-4.4 V (*vs.* Li/Li⁺), and the scan rate was 0.2 mV s⁻¹. Electrochemical impedance spectroscopy (EIS) curves were carried out on a BioLogic VMP3 system with the typical frequency range from 100 kHz to 10 mHz by applying the applied voltage of 5 mV.

First-principle calculations

The first-principle calculations are carried out by VASP code^[1, 2] based on density-functional theory (DFT)^[3, 4]. A generalized gradient approximation (GGA) using the spin-polarized Perdew-Burke-ernzerhof (PBE)^[5] scheme is used to describe the exchange-correlation

energy. The core electrons are represented by the projected enhanced wave (PAW) potential^[6]. The kinetic energy cutoff above 500 eV and the K point sampling on the heterojunction interface cell are $7 \times 5 \times 1$. Structural optimization was performed with a force convergence criterion of 0.01 eV/Å and an energy convergence criterion of 10^{-6} eV. Mo₂C crystallizes with a hexagonal structure and the optimized structural parameters ($a = b = 6.073$ Å, $c = 4.724$ Å, $\beta = 120^\circ$) used in this work were in good agreement with experimental and other theoretical values. The simulated lattice parameters of Mo were $a = b = c = 3.169$ Å. A slab model composed of (001) surface and Mo₂C (110) was constructed to simulate the Mo/Mo₂C heterojunction.

- 1 G. Kresse and J. Furthmuller, *Comput. Mater. Sci.* **1996**, 6, 15.
- 2 G. Kresse and J. Furthmuller, *Phys. Rev. B* **1996**, 54, 11169.
- 3 W. Kohn and L. J. Sham, *Phys. Rev.* **1965**, 140, 1133.
- 4 P. Hohenberg and W. Kohn, *Phys. Rev.* **1964**, 136, 864.
- 5 P. E. Blöchl, *Phys. Rev. B* **1994**, 50, 17953.
- 6 J. P. Perdew, K. Burke and M. Ernzerhof, *Phys. Rev. Lett.* **1996**, 77, 3865.

Table S1. The fraction of different valence Mo states based on XPS curves.

States of the electrodes	Species percentage (%)				
	Mo ⁰	Mo ²⁺	Mo ³⁺	Mo ⁴⁺	Mo ⁶⁺
Pristine	10.6	30.6	22.2	10.5	26.1
Discharge	3.7	27.4	25.9	14.5	28.5
Charge	5.9	26.7	20.6	13.0	34.4

Table S2. The fitting results in terms of EIS curves.

Samples	States	R_e (Ω)	R_f (Ω)	Q_1		R_{ct} (Ω)	Q_2	
				Y	n		Y	n
3DHG-Mo-700	Pristine	20.05	56.05	1.2×10^{-5}	0.74	137.89	1.7×10^{-2}	0.61
	1 st charge	40.45	41.73	1.8×10^{-4}	0.81	195.62	1.7×10^{-2}	0.59
	1 st discharge	24.42	83.72	5.1×10^{-5}	0.87	407.93	1.5×10^{-2}	0.77
3DHG-Mo/ Mo ₂ C-800	Pristine	12.36	24.5	1.1×10^{-3}	0.52	68.94	1.2×10^{-2}	0.51
	1 st charge	15.24	34.7	3.3×10^{-4}	0.63	98.31	1.5×10^{-2}	0.65
	1 st discharge	17.84	53.2	2.1×10^{-4}	0.71	196.95	1.5×10^{-2}	0.74
3DHG-Mo ₂ C-900	Pristine	14.34	41.24	1.6×10^{-3}	0.61	98.49	1.1×10^{-2}	0.51
	1 st charge	17.23	52.16	1.5×10^{-3}	0.72	169.06	1.5×10^{-2}	0.73
	1 st discharge	24.92	68.47	1.6×10^{-4}	0.58	344.16	1.3×10^{-2}	0.71

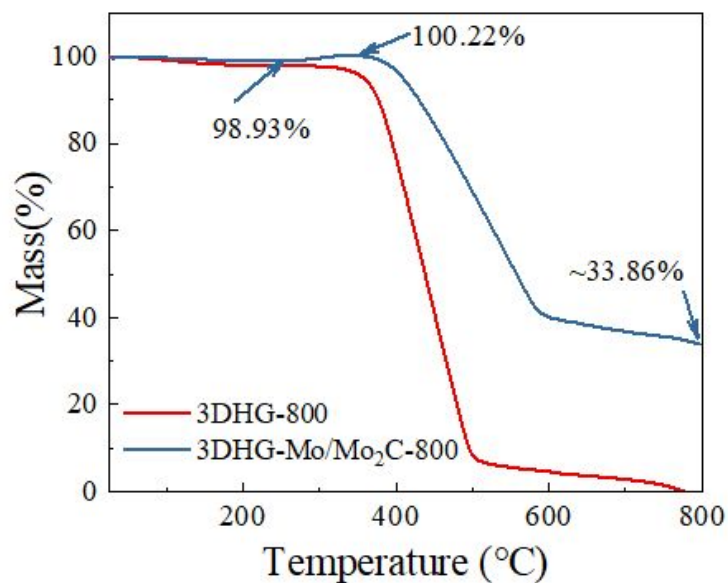


Figure S1. TGA curves of 3DHG-800 and 3DHG-Mo/Mo₂C-800, indicating that Mo/Mo₂C heterojunction was completely transformed into MoO₃ while the 3DHG-800 was transformed into CO₂.

In the TGA curve of 3DHG-Mo/Mo₂C-800, the initial weight gain from 25 °C to 240 °C is attributed to the evaporation of water (about 1.07 wt. %), and weight gain from 240°C to 340 °C is attributed to the gradual oxidation of Mo/Mo₂C heterojunction to MoO₃, followed by a weight loss caused by the combustion of 3DHG. When Mo/Mo₂C heterojunction is heated to 800 °C, it is completely transformed into MoO₃. According to these results, the Mo/Mo₂C heterojunction content is estimated to be 24.08 wt.% in 3DHG-Mo/Mo₂C-800 and the 3DHG content is calculated to be 74.85 wt. %. The weight fraction of Mo/Mo₂C might be about 2:1.

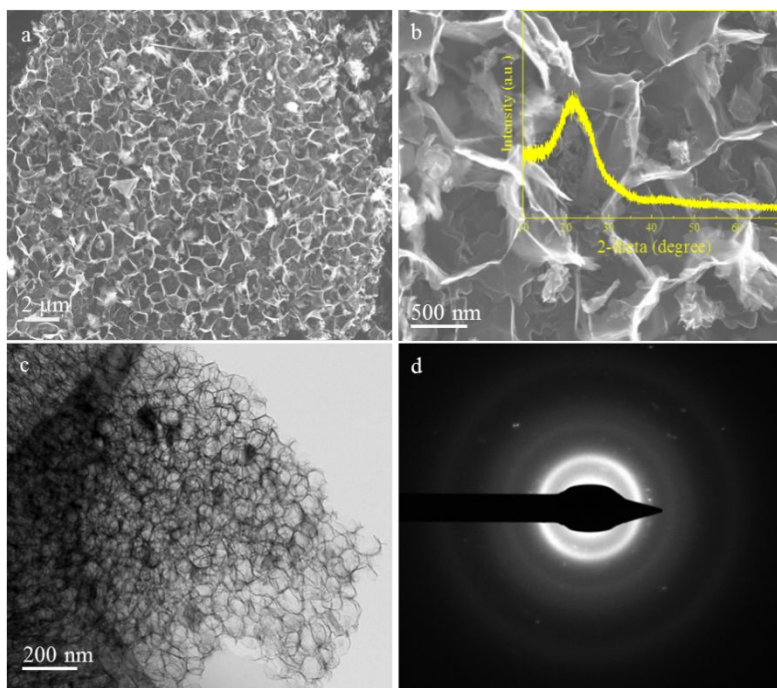


Figure S2. Characteristics of 3DHG-800. (a) SEM image, (b) enlarged SEM image (the inset is XRD pattern), (c) TEM image and (d) SAED pattern.

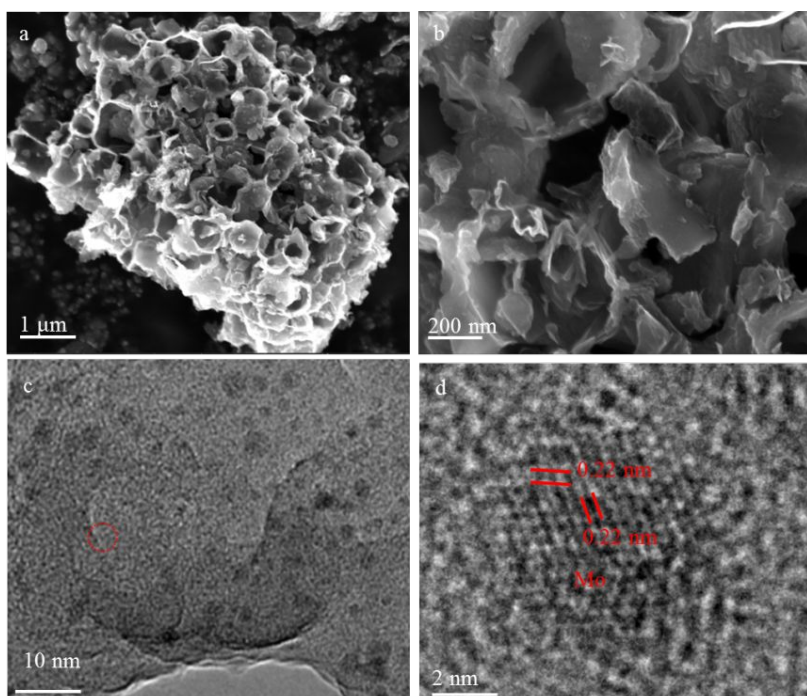


Figure S3. Characteristics of 3DHG-Mo-700. (a) SEM image, (b) High magnification SEM image, (c) TEM image and (d) HRTEM image.

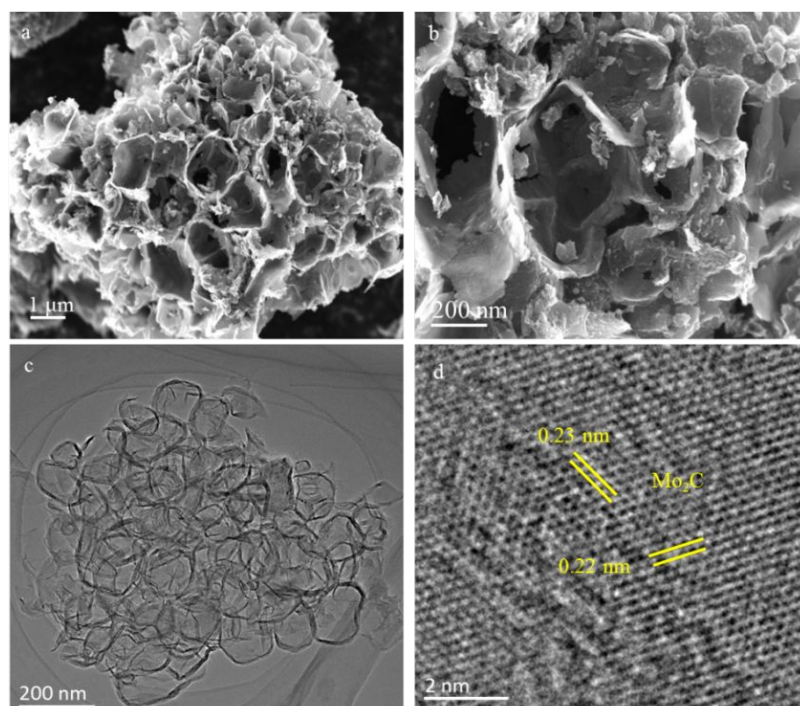


Figure S4. Characteristics of 3DHG-Mo₂C-900. (a) SEM image, (b) enlarged SEM image, (c) TEM image and (d) HRTEM image.

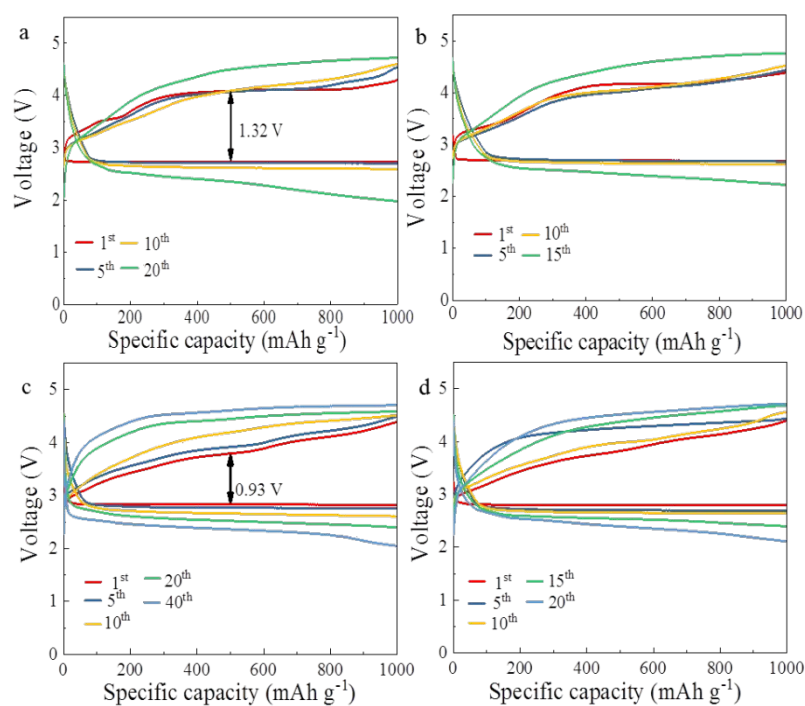


Figure S5. Electrochemical properties of LOBs based on KB and 3DHG-800. (a-b) Discharge-charge cycling stability of KB at 100 and 300 mA g⁻¹ with a cut-off capacity of 1000 mAh g⁻¹. (c-d) Discharge-charge cycling stability of 3DHG-800 at 100 and 300 mA g⁻¹ with a cut-off capacity of 1000 mAh g⁻¹.

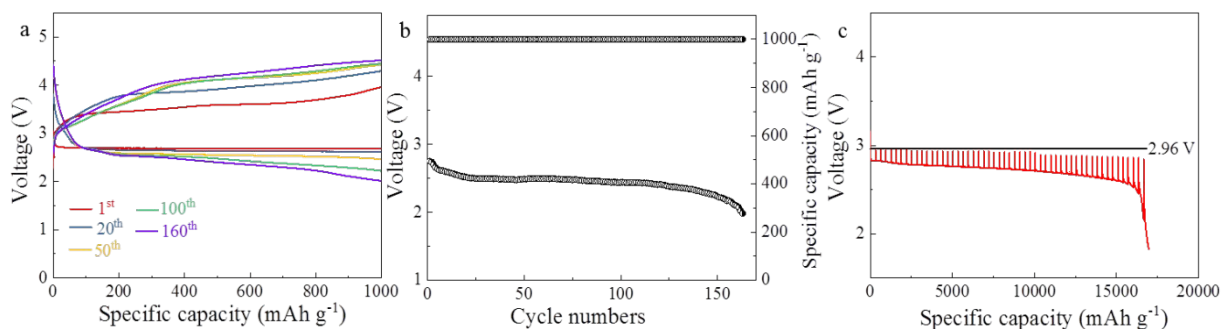


Figure S6. Electrochemical properties of LOBs based on 3DHG-Mo/Mo₂C-800. a) Discharge-charge cycling stability of 3DHG-Mo/Mo₂C-800 oxygen electrode at 300 mA g⁻¹ with a cut-off capacity of 1000 mAh g⁻¹. b) Cycling stability and terminal discharge-charge voltages of 3DHG-Mo/Mo₂C-800 cathode at 300 mA g⁻¹ with a limited capacity of 1000 mAh g⁻¹; c) Galvanostatic intermittent titration technique (GITT) of 3DHG-Mo/Mo₂C-800.

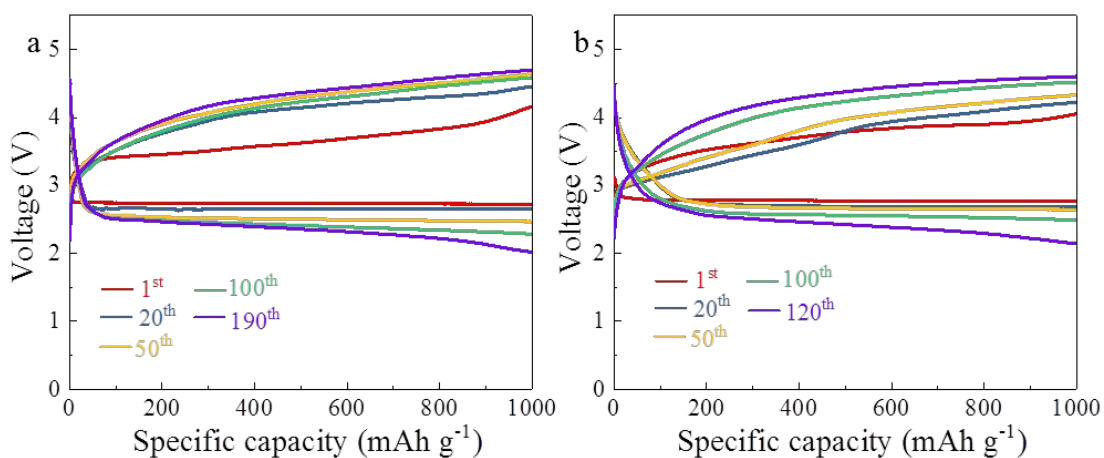


Figure S7. Electrochemical properties of LOBs based on 3DHG-Mo-700. Discharge-charge cycling stability of 3DHG-Mo-700 at 100 mA g⁻¹(a) and 300 mA g⁻¹ (b) with a cut-off capacity of 1000 mAh g⁻¹.

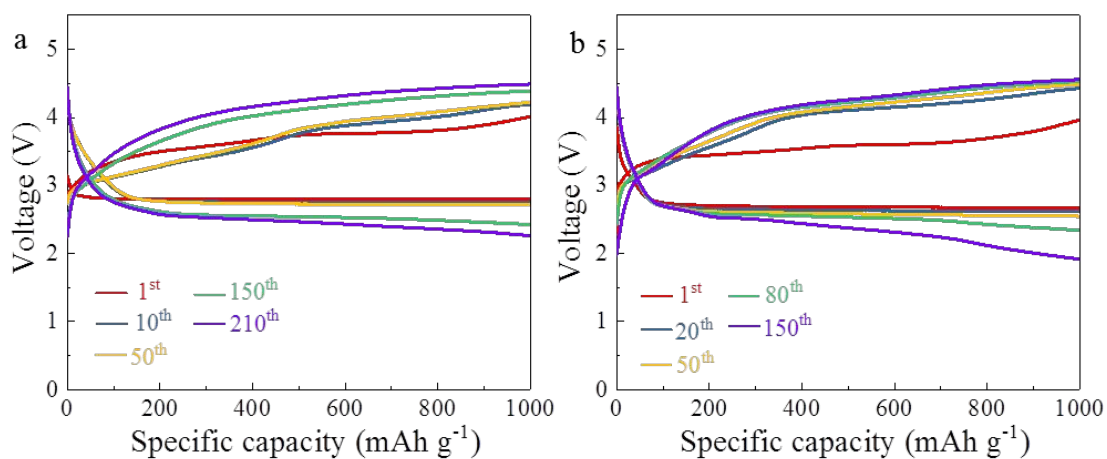


Figure S8. Electrochemical properties of LOBs based on 3DHG-Mo₂C-900. Discharge-charge cycling stability of 3DHG-Mo₂C-900 at 100 mA g⁻¹(a) and 300 mA g⁻¹ (b) with a cut-off capacity of 1000 mAh g⁻¹.

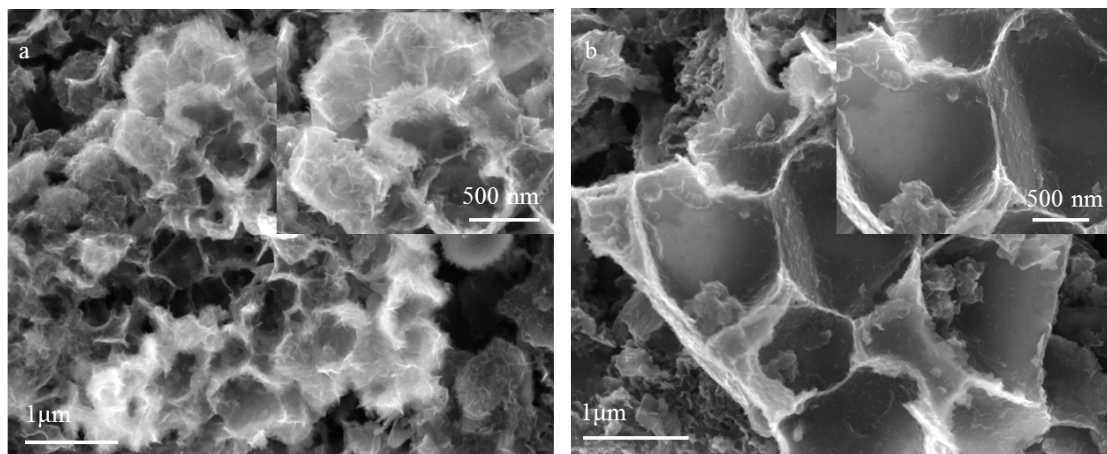


Figure S9. Typical SEM images of 3DHG-800 cathode with the 100th discharged state (a-b) and the 100th charged state (c-d), respectively.

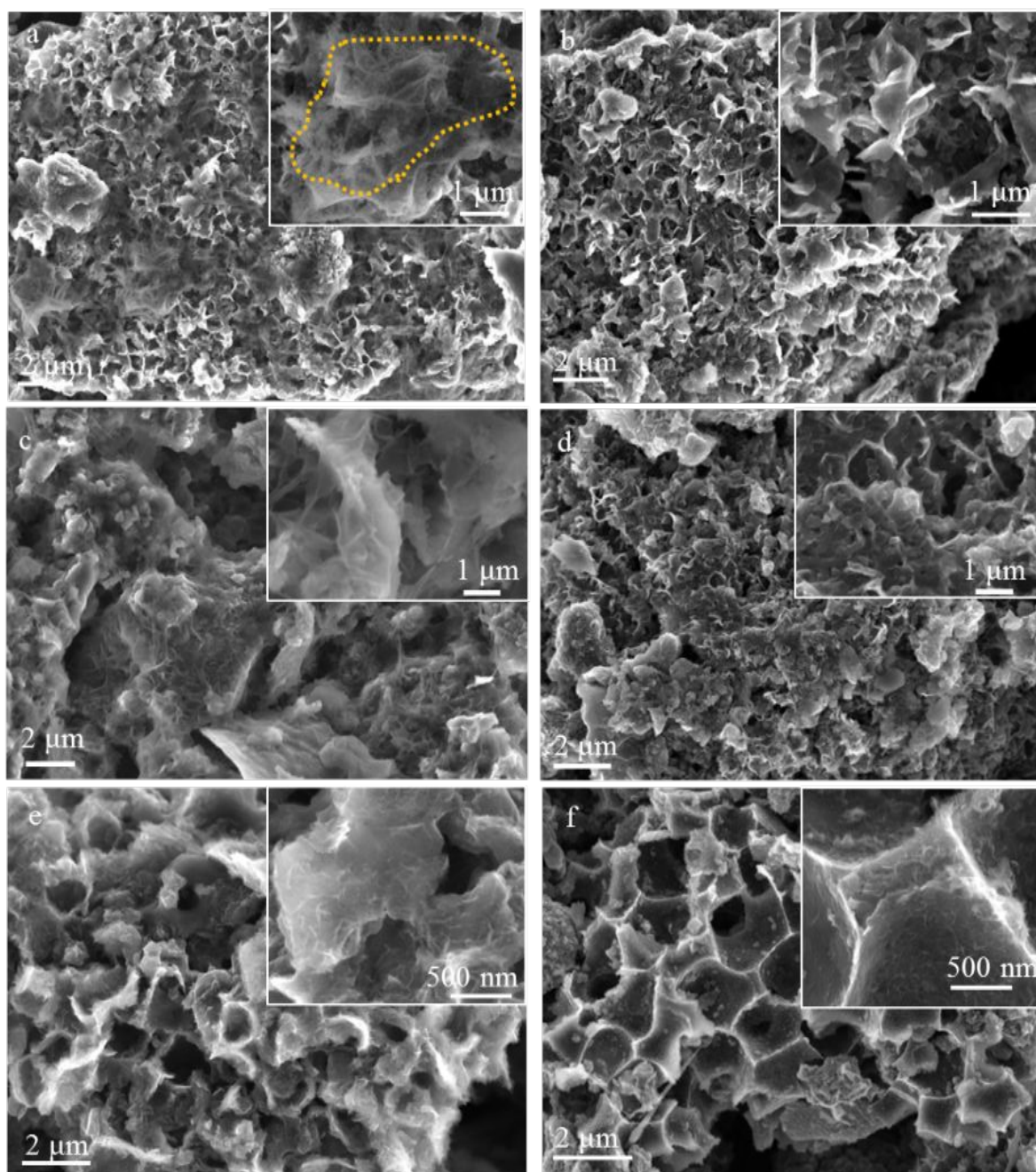


Figure S10. Typical SEM images of 3DHG-800 (a-b), 3DHG-Mo-700 (c-d) and 3DHG-Mo₂C-900 (e-f) cathodes with the first discharged state (a, c, e) and the first charged state (b, d, f), respectively.

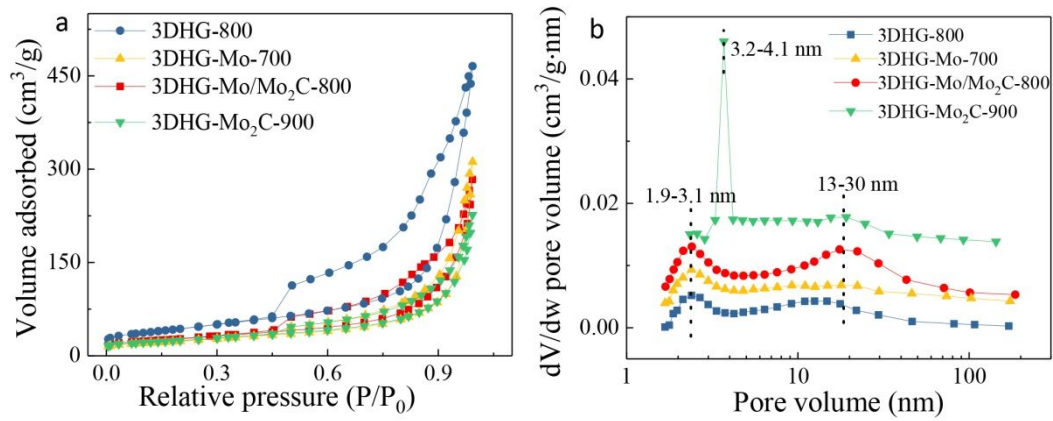


Figure S11. N₂ adsorption and desorption isotherm (a) and pore size distribution curve (b) of 3DHG-800, 3DHG-Mo-700, 3DHG-Mo/Mo₂C-800 and 3DHG-Mo₂C-900, respectively.

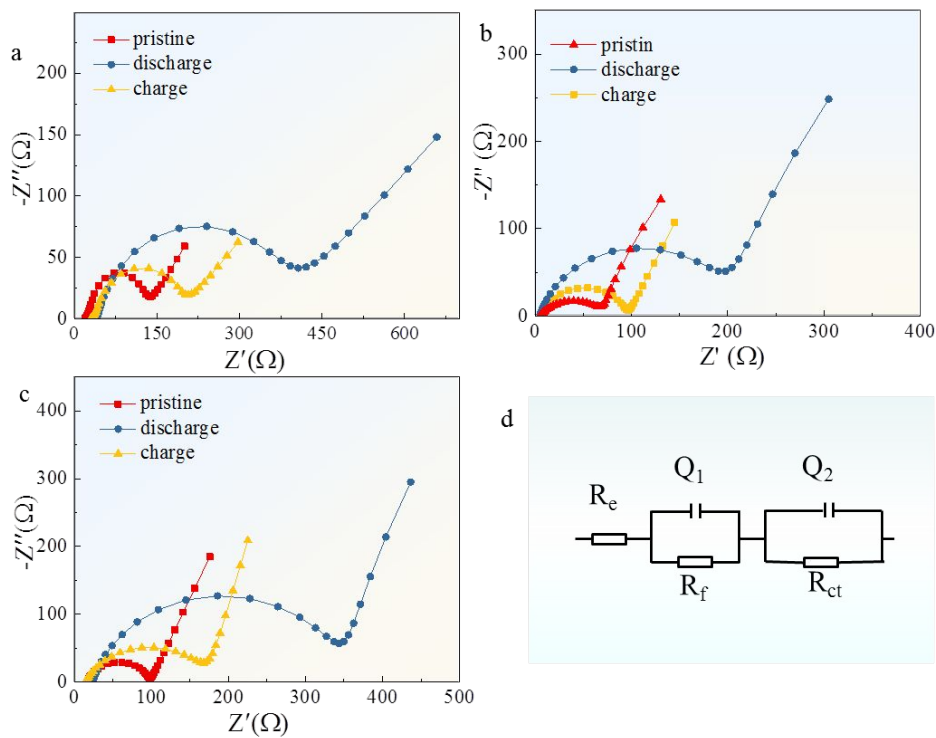


Figure S12. The electrochemical impedance spectroscopy (EIS) determined the impedance of the battery under three states of electrodes with 3DHG-Mo-700(a), 3DHG-Mo/Mo₂C-800(b) and 3DHG-Mo₂C-900 (c), (d) corresponds to the fitting circuit.